Final published version of this article in the **Journal of American Chemical Society**

Modular Assembly of Vibrationally and Electronically Coupled Rhenium Bipyridine Carbonyl Complexes on Silicon, Johannes D. Bartl*, Christopher Thomas*, Alex Henning, Martina F. Ober, Gökcen Savasci, Bahar Yazdanshenas, Peter S. Deimel, Elena Magnano, Federica Bondino, Patrick Zeller, Luca Gregoratti, Matteo Amati, Claudia Paulus, Francesco Allegretti, Anna Cattani-Scholz, Johannes V. Barth, Christian Ochsenfeld, Bert Nickel, Ian D. Sharp, Martin Stutzmann, and Bernhard Rieger

Cite this: *J. Am. Chem. Soc.* 2021, 143, 46, 19505–19516

Publication Date:November 12, 2021

https://doi.org/10.1021/jacs.1c09061

Modular Assembly of Vibrationally and Electronically Coupled Rhenium Bipyridine Carbonyl Complexes on Silicon

Johannes D. Bartl [†,‡,‖,*], Christopher Thomas [‡,‖,*], Alex Henning [†], Martina F. Ober [%,¶], Gökcen Savasci [$,+,€], Bahar Yazdanshenas [†,&], Peter S. Deimel [#], Elena Magnano [$,}], Federica Bondino [$], Patrick Zeller [{,~}], Luca Gregoratti [{], Matteo Amati [{], Claudia Paulus [†], Francesco Allegretti [#], Anna Cattani-Scholz [†,¶], Johannes V. Barth [#], Christian Ochsenfeld [$,+,€], Bert Nickel [%,¶], Ian D. Sharp [†], Martin Stutzmann [†], and Bernhard Rieger [‡]

[†] Walter Schottky Institute and Physics Department, Technische Universität München, Am Coulombwall 4, 85748 Garching bei München, Germany

[‡] Department of Chemistry, WACKER-Chair for Macromolecular Chemistry, Technische Universität München, Lichtenbergstraße 4, 85747 Garching bei München, Germany

[%] Faculty of Physics Ludwig-Maximilians-Universität München, Geschwister-Scholl-Platz 1, 80539 München, Germany

[¶] Center for Nanoscience (CeNS), Ludwig-Maximilians-Universität München, Geschwister-Scholl-Platz 1, 80539 München, Germany

[$] Max Planck Institute for Solid State Research, Heisenbergstr. 1, 70569 Stuttgart, Germany

[+] Department of Chemistry, University of Munich, LMU, Butenandtstr. 5-13, 81377 Munich, Germany

[€] Cluster of excellence e-conversion, Lichtenbergstr. 4a, 85748 Garching, Germany

[#] Physics Department E20, Technische Universität München, James-Franck-Str.1, 85748 Garching bei München, Germany

[$] IOM CNR, Laboratorio TASC S.S. 14 km 163.5, 34149 Basovizza, Trieste, Italy

[}] Department of Physics, University of Johannesburg, PO Box 524, Auckland Park 2006, South Africa

[{] Elettra-Sincrotrone Trieste SCpA, SS14-Km163.5 in Area Science Park, 34149, Trieste, Italy

KEYWORDS Hybrid semiconductor, Interface engineering, Atomic layer deposition, Aluminum oxide, Silicon, X-ray photoelectron spectroscopy, Self-assembled monolayers of phosphonic acids

ABSTRACT: Hybrid inorganic/organic heterointerfaces are promising systems for next generation photocatalytic, photovoltaic, and chemical sensing applications. Their performance relies strongly on the development of robust and reliable surface passivation and functionalization protocols with (sub)molecular control. The structure, stability, and chemistry of the semiconductor surface determine the functionality of the hybrid assembly. Generally, these modification schemes have to be laboriously developed to satisfy the specific chemical demands of the semiconductor surface. The implementation of a chemically independent, yet highly selective standardized surface functionalization scheme, compatible with nanoelectronic device fabrication, is of utmost technological relevance. Here, we introduce a modular surface assembly (MSA) approach which allows the covalent anchoring of molecular transition metal complexes with sub-nanometer precision on any solid material by combining atomic layer deposition (ALD) and selectively self-assembled monolayers of phosphonic acids. ALD, as an essential tool in semiconductor device fabrication, is used to grow conformal aluminum oxide activation coatings, down to sub-nanometer thicknesses, on silicon surfaces to enable a selective step-by-step layer assembly of rhenium(I) bipyridine tricarbonyl molecular complexes. The modular surface assembly of molecular complexes generates precisely structured spatial ensembles with strong intermolecular vibrational and electronic coupling, as demonstrated by infrared spectroscopy, photoluminescence, and X-ray photoelectron spectroscopy analysis. The structure of the MSA can be chosen to avoid electronic interactions with the semiconductor substrate to exclusively investigate the electronic interactions between the surface-immobilized molecular complexes.

Introduction. Advances in high-performance semiconductor electronic devices depends strongly on the development of robust and reliable surface passivation and functionalization schemes[1]. This is especially evident for next generation photocatalytic and photovoltaic devices[1], where inorganic semiconductor interfaces functionalized with small organic molecules are promising hybrid systems[2-5]. Surface structure, stability, and chemistry of the semiconductor generally determine the functionality of the hybrid device and its relevance for specific applications[1,6]. The ability to tailor the chemical and electronic properties of semiconductors *via* the surface chemistry with molecular control has, thus, become a driving force behind the development of state-of-the-art semiconductor technology. Although a plethora of different surface modification and functionalization schemes are available, they are specific to the unique

surface properties of the individual materials[6-9]. This specificity limits the application range of established surface functionalization approaches, including cycloaddition and dissociation chemistry, carbonization, oxidation, and hydrolytic condensation reactions, as well as hydrosilylation and various other wet chemical approaches[6,9-11]. A standardized surface functionalization approach, which circumvents the limitations of material-specific functionalization routes, is of utmost technological relevance in order to streamline the fabrication and development of hybrid inorganic/organic heterointerfaces. Different from a static bottom-up functionalization, which adapts to the surface chemistry of the semiconductor[6,12], a dynamic approach relies on the modification of the semiconductor to adopt a specific surface chemistry[1,6,12].

In this work, we introduce a modular surface assembly (MSA) approach to covalently anchor molecular complexes with sub-nm precision on solid substrates (**Scheme 1**) by tailoring the surface chemistry of silicon (Si), which remains the most relevant technological semiconductor[13]. To this end, we employ atomic layer deposition (ALD) to grow ultrathin and conformal aluminum oxide (AlO_x) coatings (ranging from 3 to ~ 0.3 nm) on Si substrates **(a)**, effectively altering its surface chemistry to enable phosphonic acid (PA) grafting *via* simple immersion **(b)**. Ultrathin AlO_x films have been applied in the photovoltaics industry, *e.g.*, for the field-effect passivation of contacts in Si solar cells[14,15], but also to improve stability and interfacial charge transport in devices based on emerging materials such as planar perovskites and two-dimensional materials[16]. However, these coatings have not yet been applied as universal activation layers for functional hybrid inorganic/organic heterointerfaces on a large scale. The PA grafting introduces a stable hydroxyl functionality (OH reactive sites) to the terminal surface, which is subsequently used to covalently attach molecular transition metal complexes (here, rhenium(I) bipyridine tricarbonyl moieties) to the functionalized Si surface *via* a mild Steglich esterification reaction **(c)**.

Scheme 1. Modular surface assembly (MSA) approach *[1]*

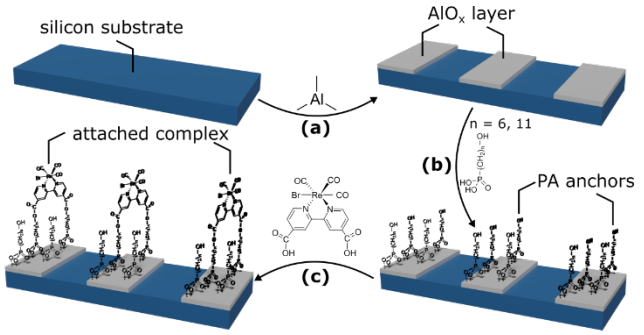

[1] The Si substrate is covered by a micropatterned aluminum oxide (AlO_x) activation layer of variable thickness (3 to ~ 0.3 nm) **(a)**, followed by area-selective surface grafting of a functional phosphonic acid (PA) anchor layer with a variable backbone **(b)**. Finally, molecular transition metal complexes (here, rhenium(I) bipyridine tricarbonyl moieties) are attached to the underlying PA anchor layer *via* a Steglich esterification reaction **(c)**, finalizing the fabrication of the modular surface assembly (MSA).

Such a step-by-step layer assembly circumvents unwanted steric and electrostatic effects induced by the molecular complexes during direct surface functionalization, which is a common strategy for the fabrication of dye-sensitized solar cells[17-20], and generates a highly ordered hybrid functional interface. Due to the modular character of this approach, individual components of the hybrid interface such as the semiconductor substrate, PA anchor, auxiliary coupling agents, and molecular complex can be flexibly modified and tuned to the requirements of the device.

We utilize highly *p*-doped Si (>$1.2 \cdot 10^{19}$ cm^{-3}; degenerate doping) to minimize electronic effects between the substrate and the molecular complexes to freely investigate intercomplex interactions. Furthermore, we focus on self-assembled monolayers of phosphonic acids (SAMPs) as organic functional anchors due to their high thermal and hydrolytic stability compared to other self-assembled monolayers (SAMs), such as silanes[21]. In addition, we exploit the poor reactivity of Si with PAs to achieve a spatially selective functionalization. PA surface chemistry with native silicon oxide (SiO_x) is only accessible *via* specific reverse Langmuir-Blodget techniques, *i.e.*, tethering by aggregation and growth (T-BAG)[22], which is specifically designed for SAMPs deposition on technologically relevant metal oxides such as ITO[23], TiO_2[24], and ZnO[25]. However, suffer from elaborate and time-consuming experimental requirements. By contrast, PAs strongly bind to AlO_x surfaces[26,27]. The concept of target-site selectivity was initially introduced by Laibinis *et al.*[28] by defining the term "orthogonal" SAMs, which sparked the development of a plethora of orthogonal chemical transformations, comprehensively discussed in ref. *(29)*. Rhenium(I) bipyridine tricarbonyl complexes and their derivates have been utilized for photo- and electrocatalysis[30-32], dye-sensitized solar cells[33,34], sensing[35], and as model systems for elucidating charge injection into semiconducting materials[36-38].

We couple these molecular complexes onto PA-functionalized surfaces to investigate intercomplex interactions. Through the MSA approach, localized ensembles with strong intermolecular vibrational and electronic coupling are generated and placed at a controlled distance to the substrate surface with sub-nm precision. Furthermore, precise lateral structuring of the molecular complexes is demonstrated on lithographically patterned Si with sub-nm thin AlO_x. The influence of the backbone spacer length on the apparent substrate/complex distance, the degree of molecular order, and the strength of vibrational and electronic coupling between the molecular complexes is investigated by comparing PAs of two different alkyl chain lengths (C_{11} and C_6). The chemical structure and nomenclature of these materials are presented in **S0**.

Results and Discussions. As a starting point to elucidate the MSA approach, we assessed the structure and configuration of the different functional coatings. **Figure 1** shows tapping mode atomic force microscopy (AFM) micrographs from a series of Si substrates at each stage of the MSA approach (see **Scheme 1**). Conformal coatings are formed for all MSA stages without indication of (pin)holes to within the resolution of the AFM (tip radius of ~ 8 nm). The surface roughness does not increase during the combined AlO_x growth and oxygen plasma surface activation step, which is important since the surface roughness is a key parameter, determining the interface quality of integrated

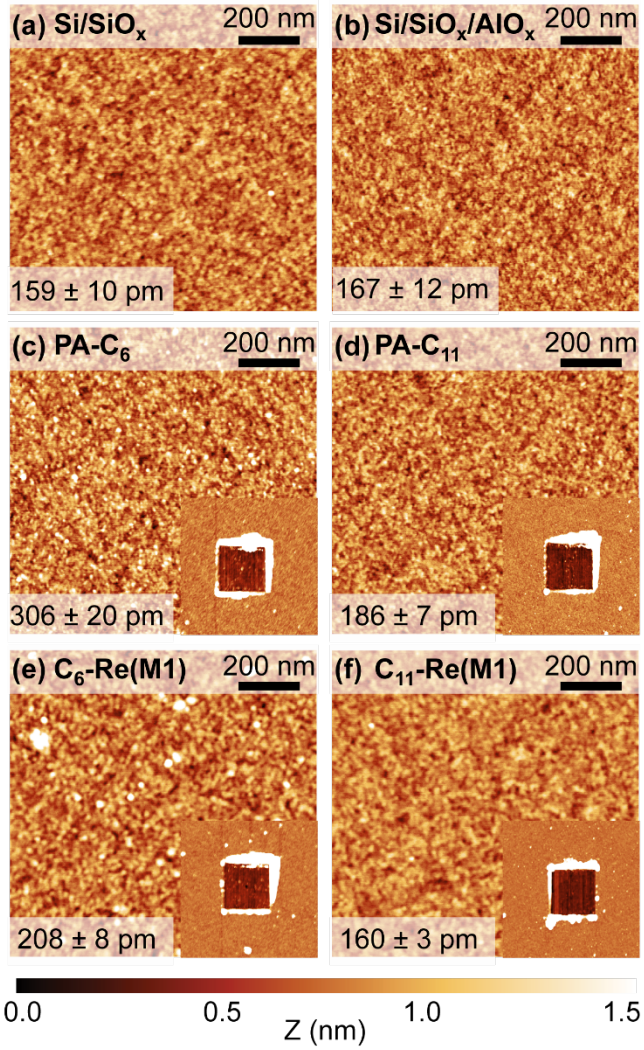

Figure 1. Tapping mode AFM micrographs (1 × 1 μm^2) from a series of Si substrates after solvent cleaning and before ALD growth **(a)**, after deposition of 3 nm AlO_x and *in-situ* oxygen plasma activation **(b)**, after surface functionalization with PA-C_6 **(c)** and PA-C_{11} **(d)**, and after Re(M1) attachment to form C_6-Re(M1) **(e)** and C_{11}-Re(M1) **(f)**. RMS roughness values were averaged over at least 3 regions distributed over the same sample. The insets show the removal of ~ 1 × 1 μm^2 of the organic overlayer in contact AFM mode.

systems and heterostructures[39]. However, the surface roughness of the PA-C_6 (306 ± 20 pm) is significantly higher than that of the PA-C_{11} anchors (186 ± 7 pm), which is attributed to a higher degree of disorder in the PA-C_6 layer. For SAMs consisting of saturated aliphatic alkyl backbones, the degree of order scales with the length of the alkyl chain, which has been attributed to the larger strength of intermolecular interactions[40,41]. Surprisingly, the surface roughness decreases upon complex (Re(M1)) attachment to the PA-C_6 anchor by 98 ± 22 pm. The effect is less pronounced for the PA-C_{11} layer, but still discernible since the Root Mean Square (RMS) roughness decreases to the initial values found on the bare Si substrate. Contrary to expectation, disorder in the PA anchor layer is only partially translated to the subsequently attached Re(M1) layer. The Re complexes possess bipyridine ligands with an extended π-system (**SI Scheme 1**), which can form strong π-π stacking interactions if a favorable surface orientation is adopted[42]. Our results indicate, that the surface morphology of the Re(M1) terminal layer is predominantly defined by such interactions, which is further elucidated by X-ray reflectivity (XRR) and near edge X-ray absorption fine structure (NEXAFS) analysis (*vide infra*). The thickness, d_{OL}, and the molecular tilt angle, θ, of the organic constituents were determined from the measured step height after removal of the organic layer using contact mode AFM as shown by the insets in **Figure 1** and explained in detail in **S3**. The thickness of the Re(M1) terminal layer, determined by subtracting the PA layer thickness from the total thickness of the assembly, appears to be primarily independent of the anchor layer thickness (**Table 1**), further indicating that its structural properties are governed by intermolecular interactions within the metal complex layer.

Complementary XRR measurements were performed to verify the AFM-derived thickness at the macro scale and to probe the internal structure of the MSA layers. **Figure 2a** shows normalized XRR curves as a function of the momentum transfer, q, from C_6-Re(M1) (blue) and C_{11}-Re(M1) (cyan) on 3 nm AlO_x-coated Si substrates. The measured reflectivity is presented together with simulated intensities based on a four-layer slab model on top of the Si substrate (solid lines), which is described in detail in **S5**. The relatively large scattering cross section of the Re metal centers gives rise to a pronounced Gaussian-shaped scattering length density (SLD) profile (orange, **Figure 2b**), indicative of a highly ordered surface layer for both PA anchors. We note that the FWHM difference between the SLD Gaussian profiles falls within the inner layer resolution of ~ 4 Å and does not allow a quantitative estimate of the relative degree of order. Conversely, the distance between the Re centers and the substrate surface can be determined with high precision, as reflected by the small corresponding errors. This distance was calculated by the spacing between the Gaussian peak center and the inflection point of an error function, representing the Si/AlO_x substrate (combined fit shown as solid lines in **Figure 2b**), which results in 1.03 ± 0.01 nm and 1.51 ± 0.01 nm for C_6-Re(M1) and C_{11}-Re(M1), respectively, consistent with AFM results (**Table 1**). Thus, the reflectivity data suggest that the different organic layers are, indeed, homogeneously distributed over the whole sample surface. It is also confirmed that the PA layers do not only act as simple anchors, but also as efficient

Table 1. Overview of the organic layer thickness determined by AFM and XRR, along with the molecular tilt angles obtained by AFM and NEXAFS measurements. All tilt angles are given with respect to the surface normal.

Si/AlO_x (3nm)	**d_{OL} (nm) (AFM)**	**d_{OL} (nm) (XRR)**	**$d_{Re(M1)}$ (nm) (AFM)**	**θ (°) (AFM)**	**α_N (°) (NEXAFS)**
C_6-Re(M1)	1.11 ± 0.15	1.03 ± 0.01	0.53 ± 0.17	54.9 ± 0.2	34 ± 7
C_{11}-Re(M1)	1.56 ± 0.13	1.51 ± 0.01	0.59 ± 0.16	50.2 ± 0.2	38 ± 7

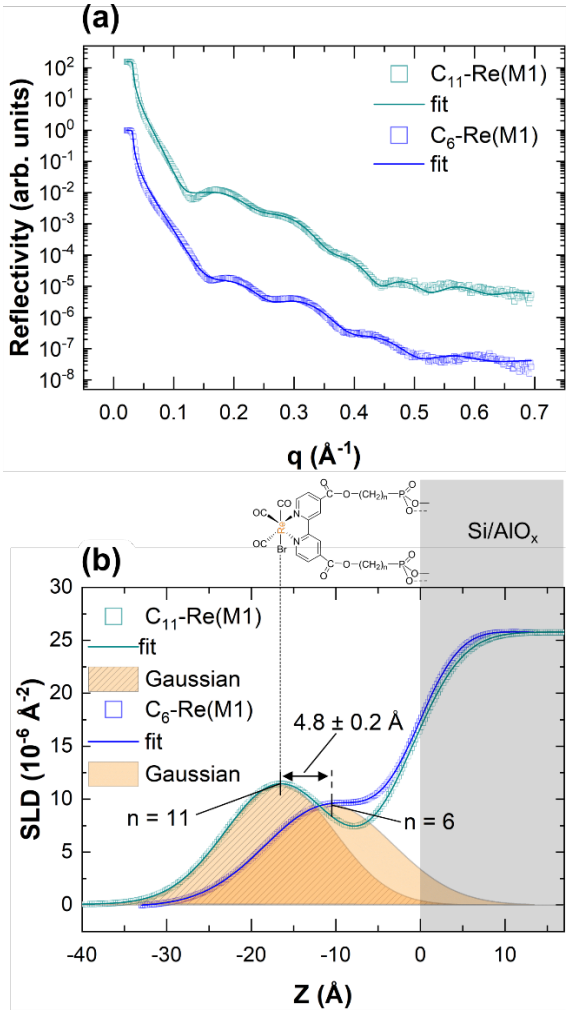

Figure 2. Normalized XRR curves as a function of the momentum transfer, q, of C_6-Re(M1) (blue) and C_{11}-Re(M1) (cyan) on 3 nm AlO_x-coated Si substrates **(a)**. For clarity, the curves are shifted vertically along the intensity axis. The measured reflectivity is presented together with simulated intensities based on a four-layer slab model on top of the Si substrate (solid lines), which is described in detail in **S5**. All model-related parameters are summarized in **SI Table 3**. SLD profiles are well described by a Gaussian peak fitting solution (orange) **(b)**. The contribution of the Si/AlO_x substrate to the SLD profile is highlighted in grey.

barrier and spacer layers, effectively localizing the molecular complexes at a well-defined distance from the substrate surface, which increases by 0.10 ± 0.02 nm per CH_2-group present in the PA alkyl-backbone.

To investigate the long-range order of the molecular complexes and determine their surface orientation, we performed NEXAFS measurements. The strong and relatively sharp 1π* resonance, found at ~399.3 eV attributed to a N 1s → π* transition of the aromatic nitrogen in the bipyridyl moiety, was used to evaluate the surface orientation of the molecular complexes (**SI Figure 6**). Both modular assembled and a directly attached Re complex (C_1-Re(M0); **SI Scheme 1**) exhibit a small, but measurable dichroism, indicating, on average, a preferential ordering in the complex layers. Since C_1-Re(M0) exhibits a comparable dichroism to C_6-Re(M1) and C_{11}-Re(M1), the apparent ordering in the Re layers is attributed to π-π stacking between individual bipyridyl moieties[42], which implies the structural feasibility of electronic interaction between individual molecular complexes over the bipyridine ligands. Following the method described in **S6**, the NEXAFS-derived molecular tilt angle with respect to the surface normal, α_N, of 34°, 38°, and 32° is obtained with an empirically estimated accuracy of ± 7° for C_6-Re(M1), C_{11}-Re(M1), and C_1-Re(M0), respectively. These values differ from AFM-derived molecular tilt angles, θ, (**Table 1**), suggesting that the attachment of the Re(M1) layer introduces a structural rearrangement to the underlying PA anchors. This difference is higher for C_6-Re(M1), which is in qualitative agreement with the observed surface roughness decrease, as measured by AFM (**Figure 1**).

To deepen our analysis of the electronic properties of the MSA layers, and determine their elemental composition, coverage, and structural integrity, we conducted X-ray photoelectron spectroscopy (XPS) measurements. In **Figure 3** high resolution XPS spectra of the P 2p region are presented for the two PA anchors on 3 nm AlO_x-covered Si substrates. The PA coverages were calculated using the method suggested by Kim *et al.* (**S7**) and are listed in **Table 2**. The coverage of the two PA types is comparable and, therefore, independent of the PA backbone chain length. Apparently, disorder in the SAMPs layer, as indicated by AFM characterization for PA-C_6 (**Figure 1),** has no significant impact on the attainable surface coverage. The determined PA coverages are higher compared to experimental estimates obtained from the molar volume of phosphorus acid (4.25 nm^{-2})[43] and to the previously predicted theoretical limit of 4.3-4.7 nm^{-2} for crystalline aluminum oxide surfaces by density functional theory (DFT)[44]. However, by considering the structural dimensions of the PAs used, possible surface loadings between 1.67 and 11.24 nm^{-2} for PA-C_{11} (**S4**) are theoretically obtainable, which depend on the molecular tilt with respect to the surface normal and are limited by the size of the phosphorous head group (**SI Table 2**). This implies that the maximum achievable PA surface coverage has a stronger dependence on the amount of accessible surface binding sites than previously assumed[43,44]. Therefore, the density, morphology, and surface termination of the AlO_x activation layer are likely defining factors.

To elaborate on this hypothesis, we compared the coverage of PA-C_{11} anchors on Si substrates covered by thinner AlO_x coatings (**SI Table 4**), whose thicknesses were estimated by spectroscopic ellipsometry (SE) to be 1 nm, ~ 0.45 nm (20 ALD cycles), and ~ 0.25 nm (3 ALD cycles; sub-monolayer), respectively (**S1**). AlO_x layers below 1 nm thickness were grown by plasma-enhanced atomic layer deposition (PE-ALD) (**S1**). The PA loading on 1 nm AlO_x (5.86 nm^{-2}) is comparable to a 3 nm AlO_x layer. However, the coverage is lower on a continuous, 0.45 nm AlO_x (4.22 nm^{-2}) and, as expected, noticeably reduced on a 0.25 nm AlO_x coating (2.28 nm^{-2}). With the exception of inert metals and low energy van der Waals surfaces, thermally grown AlO_x layers are known to be continuous on hydroxylated surfaces for a layer thickness ≥ 1 nm[45], which is supported by the comparable PA coverage for 1 and 3 nm AlO_x. Due to the

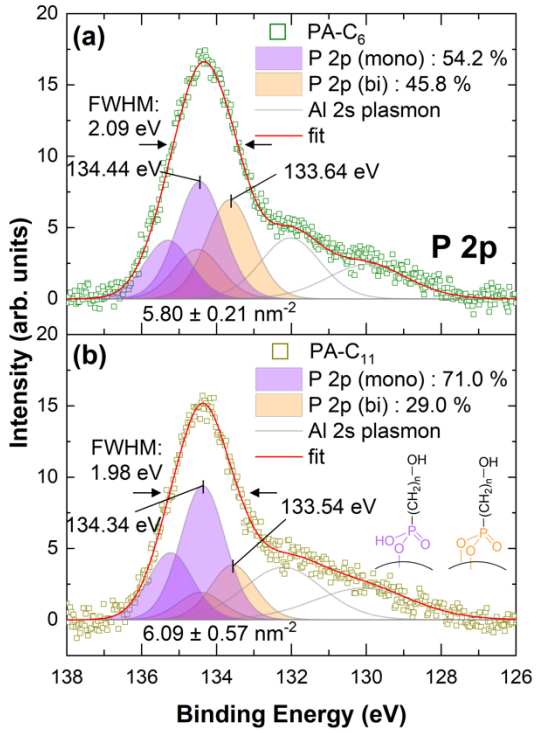

Figure 3. High resolution XPS spectra of the P 2p region for PA-C_6 **(a)** and PA-C_{11} **(b)** on 3 nm AlO_x-covered Si substrates. Components colored in light purple and light orange refer to a monodentate and bidentate binding motif, respectively (inset in **(b)**). Components colored in grey refer to Al 2s plasmon loss features.

steric hindrance of trimethylaluminium (TMA)[45], the formation of a closed AlO_x surface layer is not possible for a three-cycle growth, which is reflected by the significantly lower PA coverage on a 0.25 nm AlO_x coating. Recently[46], we demonstrated PA-C_{11} surface functionalization of a continuous, ~ 0.3 nm thick monolayer AlO_x grown on gallium nitride with a PA coverage of 4.5 ± 0.3 nm^{-2}, suggesting that the 0.45 nm AlO_x on Si is, indeed, continuous and that the PA coverage depends on the availability of AlO_x surface binding sites until a coverage of ~ 6.09 ± 0.57 nm^{-2} is reached. We note that the underlying silicon substrate is entirely inaccessible by phosphonate chemistry under the applied reaction conditions (**SI Figure 13a**).

Despite a theoretical spin-orbit splitting of 0.86 ± 0.05 eV [47,48], the P 2p peaks are broad (FWHM: ~ 2.09 and 1.98 eV for PA-C_6 and PA-C_{11}) and nearly symmetric (for PA-C_6 slightly asymmetrical to lower binding energy (BE)), which is indicative of a mixed binding motif (inset in **Figure 3b**)[49,46]. Interestingly, the best P 2p fit of PA-C_6 (**Figure 3a**) suggests a mixed binding configuration, of which the monodentate mode is slightly dominant (54.2 %), whereas for the PA-C_{11} (**Figure 3b**), a predominately monodentate (71.0 %) binding motif can be observed. We note that this distribution of binding modes was found on all measured samples (three in total for each PA type used). Previous results on atomically well-defined oxide surfaces attributed the evolution from higher to lower denticities to an increasing SAMPs surface coverage[49,50]. Since both PA coverages are similar, we conclude that the PA backbone structure influences the binding mode, even though the structural difference consists of only 5 methylene moieties. We speculate that the attainable degree of order during SAMPs formation is a decisive factor.

After attachment of the molecular complexes, three additional components can be identified in the C 1s spectrum (**Figure 4a-d**). Components C (purple), D (blue), and E (green), are attributed to bipyridine moieties, neighbors of the ester group, and carbonyl ligands, as well as the ester group, respectively. The experimentally determined carbon ratios are in good agreement with the chemical structure of the PA anchors and are slightly overestimated for the molecular complexes (**SI Table 5**), which we explain by the presence of demetallized pyridine (*vide infra*). Noteworthy, the BE of carbon moieties localized in the Re(M1) layer, are collectively blueshifted, independent of the PA anchor type, by ~ 1 eV compared to literature values[51-53], which is clearly visible for the carbon moieties of the ester groups (~ 290.15 and 290.13 eV for C_6-Re(M1) and C_{11}-Re(M1) vs. 288.8-289.3 eV[51]). In contrast, the BE of carbon moieties attributed to the PAs, *i.e.*, below the ester group (**Figure 4b** and **d)** is unaffected by this blueshift. A similar effect was observed for midchain ester-functionalized SAMs on Au{111}, for which the photoelectron kinetic energies were consistently shifted by 0.85 ± 0.03 eV between the top and bottom methylene alkyl segments independent of the relative chain lengths[54]. The effect was attributed to a strong electric dipole layer formed in the SAM. Considering the orientation of the dipole moment of the ester group (inset in **Figure 4d**) and the corresponding molecular tilt angles (57.4 ± 0.1° and 56.4 ± 0.1° vs. 31 ± 4°[54]), a correlated shift of 1.00 ± 0.01 eV and 1.00 ± 0.04 eV for C_6-Re(M1) and C_{11}-Re(M1), respectively, cannot be comprehensively explained. Notably and contrary to the results in ref. *(54)*, the BE of the ester group carbon moiety is also blueshifted by ~ 1 eV, suggesting that the effect is at least partly related to electron delocalization over the Re(M1) moiety. The presence of Re in a single chemical environment and nitrogen in two different environments is observed (**Figure 4e** and **f**). The coverage of the molecular complexes (**S7)** is roughly two times lower for C_6-Re(M1) (0.58 ± 0.02 nm^{-2}) compared to C_{11}-Re(M1) (1.08 ± 0.08 nm^{-2}) and, in both cases, lower than the highest possible coverage of 1.43 ± 0.01 nm^{-2} estimated from QCC calculations (**S4**). The lower coverage on C_6-Re(M1) is

Table 2. Overview of the PA and molecular complex surface coverage obtained from XPS measurements for different stages of the MSA approach on 3 nm AlO_x-coated Si substrates. Errors correspond to the standard deviation considering three different samples for each type.

Si/AlO_x (3 nm)	PA coverage [nm^{-2}]	Re(M1) coverage [nm^{-2}]	PA/Re(M1) ratio
C_6-Re(M1)	5.80 ± 0.21	0.58 ± 0.04	10.00 ± 0.78
C_{11}-Re(M1)	6.09 ± 0.57	1.08 ± 0.06	5.64 ± 0.61

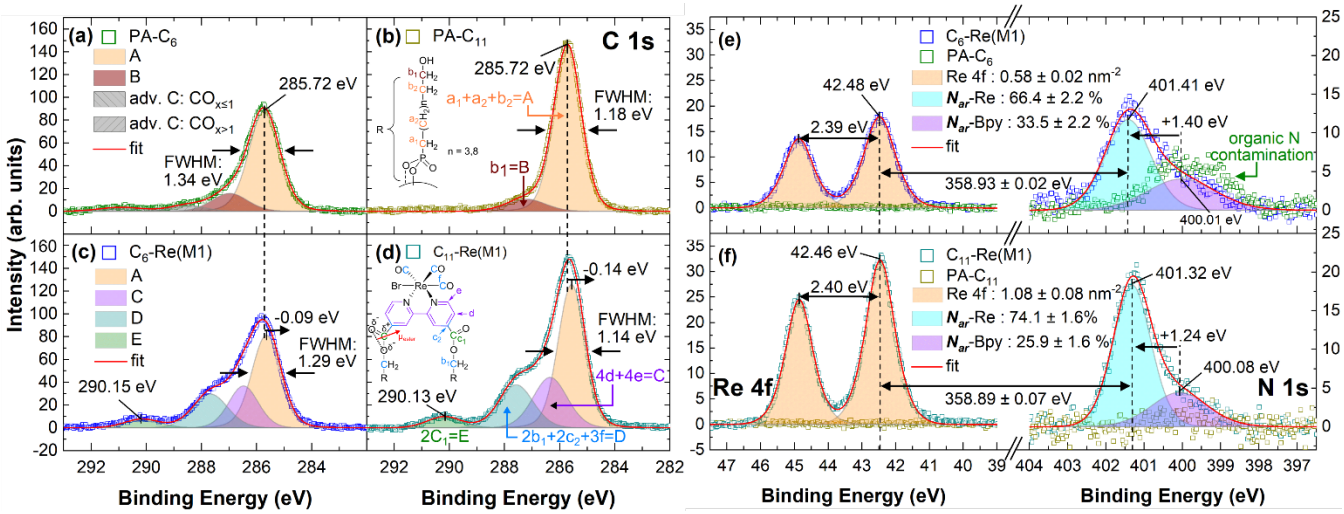

Figure 4. High resolution XPS spectra of the C 1s region, together with the best fit for PA-C_6 **(a)**, PA-C_{11} **(b)**, C_6-Re(M1) **(c)**, and C_{11}-Re(M1) **(d)** on 3 nm AlO_x-coated Si substrates. The chemical structure of the PA anchors and molecular complexes are shown as insets in **(b)** and **(d)**, respectively. The orientation of the ester group's dipole moment, μ_{ester}, is marked in red. Chemical functionalities with relative binding energy (BE) shifts of ≤ 0.3 eV (instrumental resolution) are grouped into single components (A-E). The theoretically and experimentally determined carbon ratios are summarized in **SI Table 5**. Corresponding high resolution XPS spectra of the Re 4f and N 1s region, together with the best fit solution for PA-C_6 and C_6-Re(M1) **(e)**, as well as for PA-C_{11} and C_{11}-Re(M1) **(f)**. High resolution XPS spectra of the Br 3d region are presented in **SI Figure 9**

attributed to a lower density of reactive hydroxyl terminal groups for PA-C_6, supported by a ~ 10° higher water static contact angle compared to a PA-C_{11}-coated surface (**SI Table 1**). Similar to carbon, the BE of Re $4f_{7/2}$ (42.46 and 42.48 eV for both C_6-Re(M1) and C_{11}-Re(M1)) is found ~ 1 eV higher than the expected literature value for a +1 oxidation state[52,53]). A similar BE shift was reported for structured rhenium bipyridine tricarbonyl dyes, modified by flexible or aromatic bridges and assembled on SiO_2 and TiO_2 by Langmuir-Blodgett techniques[55], but the origin of the shift was not explained. In addition, the BE difference between the lower BE (purple) and higher BE (cyan) N 1s component is ~ 1 eV (**Figure 4e** and **f**), which is consistent with the observed C 1s and Re 4f BE shift. A BE of ~ 400 eV is typical for pyridinic nitrogen[56], *i.e.*, the aromatic nitrogen of the bipyridine moiety, which we verified by XPS measurement taken from a thin layer of PA-modified bipyridine ligands (**SI Scheme 1**), deposited on an Au surface *via* drop-casting (**SI Table 6**). The amount of pyridinic nitrogen found on C_{11}-Re(M1) (25.9 ± 1.6 %) coincides well with the amount needed to achieve full surface coverage (24.5 ± 6.3 %) estimated from Quantum-Chemical Calculations (QCC) (**S4**). Therefore, we suggest that the pyridinic nitrogen component is related to a demetallized complex, *i.e.*, a molecular complex, from which the metal center is removed. The amount of pyridinic nitrogen on C_6-Re(M1) is slightly higher (33.5 ± 2.2 %), which is, however, related to minor contamination present already in the PA-C_6 anchor (**Figure 4e**).

To elucidate the origin of the correlated BE shift (**Figure 4**), a molecular complex was directly attached to a 3 nm AlO_x-coated surface (C_1-Re(M0); SI **Scheme 1**), *i.e.*, without the presence of an ester group as a coupling agent. In addition, a Ti/Pt (15/150 nm) layer was grown on top of a Si substrate by electron beam evaporation and a thin layer of uncoupled molecular complexes (Re(M1) (free); **SI Scheme 1**) was deposited on the Pt-covered surface *via* drop-casting (physisorption). **SI Table 6** shows the results of the XPS characterization. The Re $4f_{7/2}$ BE of the uncoupled complex, physisorbed on the Pt-covered substrate, is 41.45 ± 0.14 eV, which is in good agreement with a +1 oxidation state[52,53] and translates to a redshift of 1.12 ± 0.01 eV and 1.14 ± 0.05 eV compared to C_6-Re(M1) and C_{11}-Re(M1), respectively. Furthermore, the corresponding N 1s BE is 400.24 ± 0.03 eV and, thus, comparable to the nitrogen of the demetallized bipyridine moiety. Surprisingly, the observed Re $4f_{7/2}$ BE shift for C_1-Re(M0) is 0.87 eV and, thus, slightly lower than the MSA layers, but still significantly higher than an uncoupled complex. The correlated BE shifts for the MSA layers on thinner AlO_x coatings are comparable to the 3 nm benchmark (**SI Table 6**). Therefore, we conclude that while the collective BE shifts observed by XPS measurement are partly generated by the embedded dipole moment of the ester groups, they are primarily induced by electronic interactions between individual molecular complexes. In our understanding, the electron density of the Re metal centers, mainly provided by *d*-orbital contributions from the $Re(CO)_3Br$ moieties, is delocalized between two or more complexes, which is mediated by the bipyridine ligands *via* mixed electronic orbitals (π-π stacking), already partly suggested by NEXAFS measurements (**SI Figure 6**). This would also explain the BE difference between the metallized and demetallized pyridinic nitrogen of ~ 1 eV (**Figure 4**), as the primary source of electron density is lost upon decomposition of the complex, also suggesting that the demetallized bipyridine ligand does not participate in electron density distribution process. Due to the size of the Re metal center (Z = 75), a surface-immobilized, demetallized bipyridine is likely to adopt

a different surface orientation compared to the metallized complexes, which is consistent with the small dichroism determined by NEXAFS measurements (**SI Figure 6**).

We further investigated the intercomplex interactions *via* changes of the vibrational modes of bound and unbound molecular complexes by attenuated total reflectance Fourier-transform infrared (ATR-FTIR) spectroscopy **(Figure 5).** A sketch of the three characteristic Re-carbonyl (CO) vibrational stretching modes, *i.e.*, the in-phase symmetric, a′(1), antisymmetric a″, and out-of-phase symmetric a′(2) stretch are presented in the bottom, right corner of **Figure 5**. The maxima and relative intensities of the Re-CO vibrational modes of C_6-Re(M1) and C_{11}-Re(M1) are comparable and, therefore, independent of the chain length of the PA anchor, suggesting no vibrational interactions with the underlying substrate as previously observed on TiO_2 surfaces[28]. However, the vibrational spectra are appreciably different from the unbound molecular complex (C_{11}-Re(M1) (free)) (**Figure 5a**). Two Gaussian components (orange)[57] were used to fit the a′(1) vibrational mode of the surface-bound complex to account for the doublet structure observed for C_{11}-Re(M1) (free). Compared to the unbound complex, the a′(1) doublet feature is slightly broadened and the doublet intensity ratio is inverted. However, the vibrational energies are nearly identical. Conversely, the signal intensity of the a′(1) relative to a″ and a′(2) of the surface-bound complex is significantly increased compared to that of the unbound complex, indicating that an in-phase symmetric stretch is strongly favored over an antisymmetric or out of-phase symmetric stretch. The a″ and, in particular, the a′(2) stretching modes are blueshifted, which we attribute to vibrational coupling between individual complexes as a consequence of spatial confinement upon attachment to the surface-bound PA-anchors. Similar vibrational coupling was reported, *e.g.*, for $ReCl(CO)_3(bypy)CO_2H$ clusters directly deposited on TiO_2 nanoparticles[38] and $ReCl(CO)_3(bypy)CO_2H$ / $ReCl(CO)_3(bypy)$ $(CO_2H)_2$ films on nanocrystalline TiO_2[58]. Generally, the coupling between metal carbonyl groups is large enough to excitonically delocalize the vibrations across multiple carbonyl groups on neighboring molecules[58]. In addition, these reports[38,58] suggest a blueshift for coupled vibrational modes around 10-15 cm^{-1} per Re "dimer" aggregate, *i.e.*, vibrational coupling between two surface-bound complexes. For a trimer, the vibrational energies would increase further by ~ 10 cm^{-1}. Judging from the observed blue shift for both MSA layers (~ 9-18 cm^{-1}), the vibrational coupling is most likely reserved to only two adjacent Re complexes. We note that the vibrational energies and relative intensities of the Re-CO vibrational modes are stable up to ~ 58 d, *i.e.*, on a month scale (**SI Figure 10d**), indicating the stability of the vibrational coupling and, thus, Re terminal layers. We further note that the position of the C=O stretching mode relative to the ester group of C_{11}-Re(M1) (free), identical for the surface-bound molecular complexes (1728.9 cm^{-1}) (**Figure 5b**), confirms that both carboxylic acids modifications of Re(M1) are involved in the covalent attachment of the molecular complexes.

To substantiate our analysis of the intercomplex interactions, we performed photoluminescence (PL) measurements on C_{11}-Re(M1) (free) dissolved in DMF and C_{11}-Re(M1) assembled on

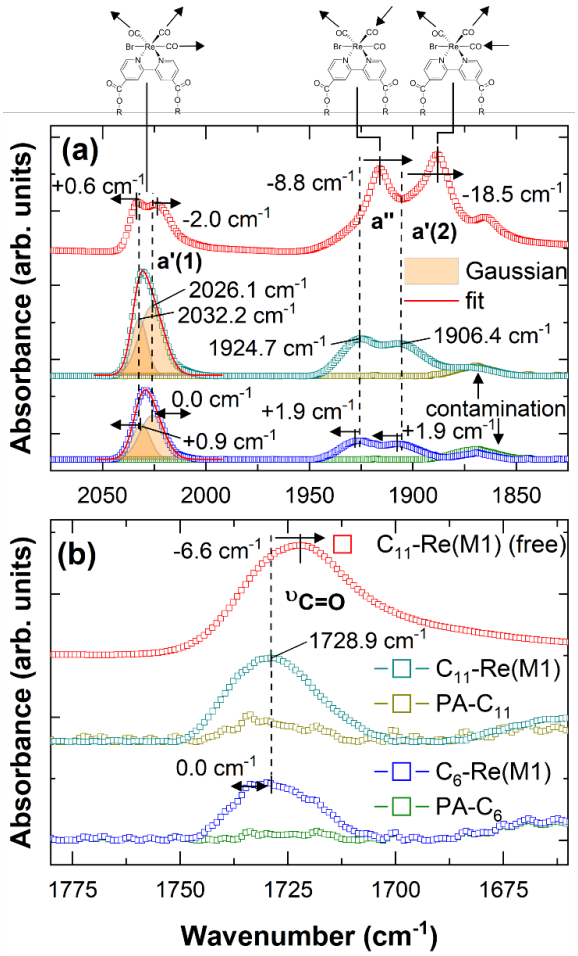

Figure 5. ATR-FTIR spectra of the three Re-carbonyl (C=O) stretching modes **(a)**, as well as the C=O stretching mode from the ester moiety **(b)**, presented for an unbound molecular complex coupled to PA-C_{11} anchor molecules (C_{11}-Re(M1) (free); red), as well as for PA-C_{11} (dark yellow) and C_{11}-Re(M1) (cyan) and for PA-C_6 (green) and C_6-Re(M1) (blue) on 3 nm AlO_x-covered Si substrates. For clarity, the IR spectra are shifted vertically along the intensity axis. A sketch of the three Re-CO vibrational stretching modes, *i.e.*, the in-phase symmetric a′(1), antisymmetric a″, and out-of-phase symmetric a′(2) stretch, are shown at the top of **(a)**. The spectrum of C_{11}-Re(M1) (free) was taken from a powder. A corresponding comparison between an uncoupled and a coupled molecular complex can be found in **SI Figure 10**.

a 3 nm AlO_x-covered Si substrate (**SI Figure 11**). Modular assembly of the Re(M1) promotes a blueshift of the PL emission of ~ 30 nm.Recently, blueshifted emissions arising from π-π stacking interactions between two nitrogen-donor ligands was reported for luminescent rhenium tricarbonyl complexes[59], suggesting that charge-transfer, mediated by π-π stacking between individual bipyridine ligands, is feasible. We conclude that the observed collective BE blueshift observed by the XPS measurements (**Figure 4** and **SI Table 6**) is, indeed, related to charge-transfer between individual Re metal centers. To our

knowledge, this is the first time that XPS has been used to establish a quantitative connection between vibrational and electronic coupling of surface assembled rhenium(I) bipyridine tricarbonyl molecular complexes. Since no dependence of the PA or AlO_x layer thickness could be observed either by XPS or ATR-FTIR measurements, the observed phenomena are purely related to intercomplex interactions. Furthermore, the strength of the intermolecular coupling (either vibrational or electronic) appears to be independent of the molecular complex surface coverage, suggesting that a lower threshold aggregation density, for which such interactions are diminished or even suppressed is not reached for coverages of $\geq 0.58 \pm 0.04$ nm^{-2}.

To evaluate the selectivity of the MSA approach, we applied a low-temperature PE-ALD process compatible with photolithography (**S1**) to create an AlO_x micropattern on a Si substrate. The surface topography of the AlO_x-patterned substrate, evaluated by AFM, is presented in **SI Figure 12**. As a proof of concept, we opted to use PA-C_{11} anchors due to the higher order in the SAMPs and the higher surface coverage of the molecular complexes. Scanning photoelectron microscopy (SPEM) measurements were performed to elementally map the micropatterned and functionalized substrates. The spatial resolution (~ 150 nm) is notably higher than for laboratory-based XPS setups, which allowed the characterization of core level emission from individual stripes (~ 4 µm in width) of the AlO_x-patterned surface. **Figure 6** shows Al 2p **(a)** and Re 4f **(b)** SPEM maps of C_{11}-Re(M1) on an AlO_x-patterned *n*-type Si substrate. The characteristic Re 4f signal of the molecular complex (bottom part of **Figure 6c**) is exclusively found on the AlO_x, which uniformly

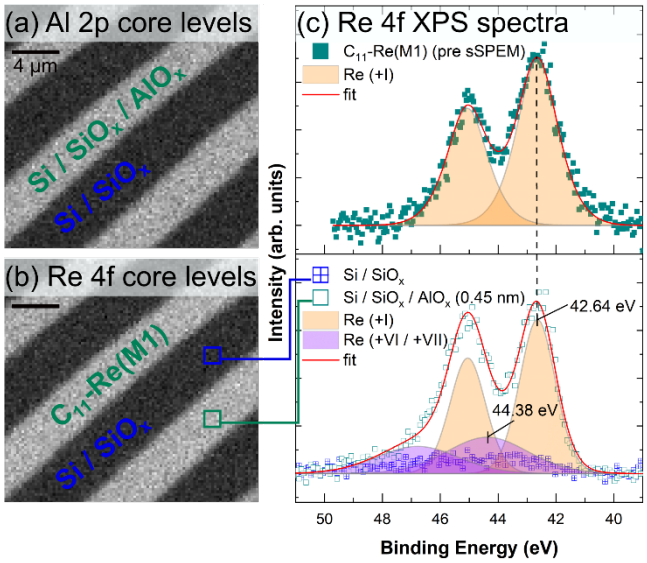

Figure 6. SPEM Al 2p **(a)** and Re 4f maps **(b)** of C_{11}-Re(M1) on an AlO_x-patterned, *n*-type Si substrate and corresponding Re 4f spectra (bottom graph in **(c)**) obtained from the areas indicated in **(b)**. For comparison, a Re 4f spectrum of the same sample prior to SPEM characterization obtained by conventional XPS is shown in the top graph of **(c)**. The characteristic Re 4f signal of the molecular complex is exclusively found on the AlO_x covered parts, uniformly following the pattern of the adhesive layer (bottom graph of **(c)**).

follows the pattern of the activation layer, demonstrating that the MSA was formed selectively on the AlO_x micropattern. We note that the SPEM-derived Re 4f spectrum shows a tail to higher BE, which can be fitted by a second Re species with a significantly higher oxidation state. We attribute the origin of this second species to the highly focused X-ray beam, which likely led to partial decomposition of the organic constituents of the MSA layer. For comparison, a laboratory XPS Re 4f spectrum of the same sample prior to SPEM characterization is shown in the top part of **Figure 6c**, indicating the presence of Re in only one distinct chemical environment.

Conclusion and Outlook. With the modular surface assembly (MSA) approach, investigated in this work, a stable and area-selective functionality can be introduced to any solid substrate independent of the specific chemical affinity of the surface. As a proof of concept, MSA layers based on rhenium(I) bipyridine tricarbonyl moieties are placed with sub-nanometer precision on aluminum oxide (AlO_x)-covered silicon substrates to generate precisely structured spatial ensembles with strong intermolecular vibrational and electronic coupling. We demonstrate that both the vibrational and electronic coupling are related, and that the electronic coupling can be monitored by X-ray photoelectron spectroscopy *via* a correlated shift to lower photoelectron kinetic energies of the functional groups located in the molecular complexes. By carefully selecting the structure of the MSA, electronic interactions with the semiconductor substrate can be disentangled to exclusively investigate the interactions between the surface-immobilized molecular complexes. The MSA approach can be transferred to any substrate on which a conformal aluminum oxide growth *via* atomic layer deposition is feasible. The approach combines surface passivation and surface functionalization in one step to create well-defined and scalable hybrid functional interfaces, which opens a new avenue in semiconductor device fabrication. As an example, we have recently shown that PA-C_{11} anchors can be grafted onto a monolayer AlO_x surface layer grown on gallium nitride (GaN) by PE-ALD with a high surface coverage, creating a well-defined semiconductor / dielectric / PA anchor hybrid interface[46], which motivates additional studies. Due to its high flexibility, the approach can be further expanded, *e.g.*, by inclusion of metal-polypyridyl coordination chemistry[60,61] to bridge the gap towards multiple metal-organic layers, which are highly relevant for device applications[31,62]. Furthermore, additional functionalities can be introduced on uncovered Si surface areas, *e.g.*, *via* silane chemistry[63,64] or, more specifically, *via* aryldiazonium cation reduction[65] to create a network of area-selective functionalities for applications in electronic devices, biosensors, and photovoltaic or photoelectrochemical cells. Furthermore, the conformal nature of the ALD growth and the experimentally simple chemistry of the MSA approach compels the focus on delicate, high aspect ratio, nanostructured semiconductors, *e.g.*, for sensing applications[66,67].

Experimental Section. General. Unless stated otherwise, all chemicals were purchased from Sigma-Aldrich, ABCR, or TCI Europe and used without further purification. All reactions with air- and moisture-sensitive substances were carried out under an argon (Ar) 5.0 (99.9990 %, *Westfalen AG*) atmosphere using standard Schlenk techniques. Prior to use, all glassware was

heat-dried under a vacuum. Toluene, tetrahydrofuran, and dichloromethane were dried using an MBraun SPS-800 solvent purification system and stored over 3 Å molecular sieves. Liquid chromatography-mass spectrometry (LC-MS)-grade acetonitrile and methanol were purchased from VWR. Single side polished, 381 ± 25 µm nominally thick, highly *p*-doped (B-doped, <0.005 Ω·cm (>$1.2 \cdot 10^{19}$ cm^{-3}); degenerate doping) Si (100) wafers grown by the Czochralski (CZ) method were ordered form Si-Mat (Kaufering, Germany) and diced into 1 × 1 cm^2 pieces. In addition, single side polished, 525 ± 20 µm nominally thick, *n*-doped (As-doped, <0.005 Ω·cm) Si (100) wafer grown by the Czochralski (CZ) method were obtained from SIEGERT WAFER (Aachen, Germany) and diced into 1 × 1 cm^2 pieces. Prior to any surface treatment, the diced wafer pieces were subsequently cleaned in an ultrasonic bath (37 kHz, 120 W) with acetone (Merck, VLSI Selectipur, >99.9 %), 2-propanol (BASF, VLSI Selectipur, >99.9 %), and deionized water (DI H_2O; 18.2 MΩ·cm at 25 °C, Merck Millipore) for 10 minutes, respectively, and dried under a stream of nitrogen (N_2).

Preparation of Self-assembled Monolayers of Phosphonic Acids (SAMPs). SAMPs of 6-hydroxyhexylphosphonic acid (≥98 % (GC); referred to as PA-C_6) and 11-hydroxyundecylphosphonic acid (≥99 % (GC); referred to as PA-C_{11}) (SiKÉMIA, Montpellier, France) were prepared *via* an immersion technique recently reported in detail for monolayer AlO_x grown on *c*-plane, *Ga*-polar GaN substrates[46].

Attachment of Re(2,2'-bipyridine-4,4'-dicarboxylic acid)$(CO)_3$Br (Re(M1) (free)). Re(M1) (free) was synthesized following a procedure reported in[68]. A detailed description of the synthetic route and characterization of all metal complexes is presented in **S12**. Both carbon acid modifications of Re(M1) were coupled to the OH end groups of the respective PA anchor layers *via* a mild Steglich esterification reaction[69], which we adopted and optimized accounting for the constraints of a surface reaction. The PA-functionalized wafer pieces (mounted on a Teflon sample holder) were immersed vertically in a 30 ml tetrahydrofuran (THF; anhydrous, HPLC-grade, ≥99.9 %,) solution of Re(M1) (free) (3 mg, 5.05 µmol, 1 eq), *N*-(3-dimethylaminopropyl)-*N*'-ethylcarbodiimide hydrochloride (EDCl; 29 mg, 0.15 mmol, 30 eq), and 4-dimethylaminopyridine (DMAP; 3 mg, 25 µmol, 5 eq). The reaction was stirred under light exclusion and an Ar atmosphere at 50 °C for 12 h. After the esterification reaction, the pieces were cleaned subsequently with *N,N*-dimethylformamide (DMF; Sigma-Aldrich, 99.8%), THF (Sigma-Aldrich, anhydrous, inhibitor-free, ≥99.9 %), DMF, methanol (MeOH; Sigma-Aldrich, 99.8 %), and DI H_2O in an ultrasonic bath (37 kHz, 60 W) for 5 minutes, respectively, to remove excess reactants and byproducts, dried under N_2, and stored in a desiccator (~ 10^{-2} mbar).

Attachment of Re(([2,2'-bipyridin]-4-ylmethyl)phosphonic acid)$(CO)_3$Br (C_1-Re(M0) (free)). C_1-Re(M0) (free) was synthesized following procedures presented in detail in **S12**. C_1-Re(M0) was directly attached to the *in-situ* oxygen plasma-activated AlO_x-coated substrate by vertical immersion of the wafer pieces (mounted on a Teflon sample holder) in a 40 ml ethanol (EtOH; VWR, Ethanol absolute ≥99.8 %, AnalaR NORMAPUR, ACS, Reag. Ph. Eur.) solution containing 5×10^{-4} $mol \cdot L^{-1}$ of PA-C_1-ReBpy (free) and stored for 24 h vibration-free in the dark under an N_2 atmosphere at room temperature.

Atomic Force Microscopy (AFM). Surface topography and roughness were investigated by AFM on a commercial setup (MultiMode 8, Bruker, Billerica, MA, USA) in amplitude-modulated (AM) tapping-mode (TM) under ambient conditions. In addition, the organic layer thickness was probed by AFM operated in contact mode (CM) and AM-TM. AFM "scratching" experiments were performed on a commercial setup (Nanoscope V Controller, Dimension V Controller, Bruker Nano GmbH, Berlin, Germany) operated under ambient conditions. A detailed description of AFM setups and experimental procedures is given in **S3**.

X-ray reflectivity (XRR). XRR measurements were performed on an in-house built X-ray reflectometer equipped with an Mo-source (Mo K_α = 17.45 keV) under ambient conditions. A detailed description of the setup can be found elsewhere[70]. The reflected intensity was measured by (θ-2θ) scans of sample and detector angle and corrected by subtraction of background scans with an offset angle $\Delta\theta$ of 0.1°. A beam footprint correction was performed to account for the effective beam height at low angles[71]. A detailed description of the data processing and fitting can be found in **S5**. Mean values and standard deviations are obtained by comparing two samples of two different batches.

X-ray Photoelectron Spectroscopy (XPS). XPS measurements were performed on a Kratos Axis Supra XPS setup (Kratos Analytical Ltd, Manchester, UK; base pressure ≤8×10^{-9} mbar) equipped with a monochromatic Al X-ray source (Al K_α = 1486.7 eV) operated with an emission current of 15 mA. XPS spectra were acquired in the hybrid lens mode at a pass energy (PE) of 10 eV and a take-off angle of 0°. The beam area was set to ~ 2 × 1 mm^2 using the slot collimation mode. The binding energy of the hemispherical analyzer was calibrated with *in-situ* sputter-cleaned silver (Ag 3d - 1118.51 eV), gold (Au 4f - 1402.73 eV), and copper (Cu 2p - 554.07 eV) standards (given in kinetic energy) with an accuracy of 0.025 eV. An instrumental broadening of 0.30 eV was determined by fitting the measured Ag 3d core level spectrum of an Ag calibration sample with a Voigt function[46]. No charge neutralization was performed, as no measurable binding energy shifts were observed for non-functionalized substrates). All recorded spectra were processed with CasaXPS (Casa Software Ltd, ver. 2.3.19). A detailed description of the data processing, fitting procedure, and methodology can be found in **S7**.

Attenuated Total Reflectance Fourier-Transform Infrared Spectroscopy (ATR-FTIR). ATR-FTIR measurements were performed on a VERTEX 70v vacuum FTIR spectrometer (Bruker, Billerica, USA) equipped with a liquid nitrogen-cooled MCT detector, using a grazing angle ATR accessory (VariGAT, Harrick Scientific Products, New York, USA) with a single reflection Germanium ATR crystal (Pike Technologies, Fitchburg, USA), significantly larger than the dimensions of the sample. An incidence angle of 65° was applied. Prior to measurements, samples were stored in the pumped measurement chamber overnight immediately after cleaning. All surface IR spectra were averaged over 2000 scans with a resolution of 2 cm^{-1} and background-referenced to the clean ATR crystal measured against vacuum. Data acquisition and processing were performed with the software OPUS (ver. 8.129, Bruker, Billerica, USA). For surface IR spectra a Rubberband baseline correction

was applied, and IR bands were fitted by Gaussian components to a linear background[57].

Near edge X-ray absorption fine structure (NEXAFS). NEXAFS measurements were performed at the BACH beamline at the Elettra synchrotron (Trieste, Italy) in Auger electron yield (AEY) mode using a SCIENTA R3000 hemispherical electron energy analyzer (base pressure $\leq 2\times10^{-10}$ mbar). Technical details of the BACH end station can be found in ref. *(72)*. All measurements were performed at low temperature (130-160 K) to minimize X-ray-induced damage to the organic layers. A detailed description of the data processing and methodology can be found in **S6**.

Scanning Photoelectron Microscopy (SPEM). SPEM measurements were performed at the ESCA Microscopy beamline at the Elettra synchrotron (Trieste, Italy). Technical details of the SPEM setup can be found in ref. *(73)*. The X-ray photon energy was set to 638.00 eV with a (Gaussian) X-ray focal diameter of ~ 150 nm. Elemental maps and spatially resolved spectra were taken by fixing the PE of the electron analyzer to 40 and 20 eV, respectively. Local XPS spectra were acquired by illuminating the point of interest with the submicron X-ray probe. The beamline settings resulted in an overall instrumental broadening of 0.35 eV, as determined by the Au 4f from an internal gold standard.

Quantum-Chemical Calculations (QCC). Investigated model compounds were optimized on PBE0-D3/def2-TZVP[74-77] level of theory using the TURBOMOLE[78,79] program package version V7.3.

ASSOCIATED CONTENT

Supporting Information. Introduced nomenclature (**S0**); detailed descriptions of experimental procedures and supplementary figures and tables (ALD growth and *in-situ* SE (**S1**), water SCA measurements (**S2**), AFM (**S3+10**), QCC (**S4**), XRR (**S5**), NEXAFS (**S6**), XPS (**S7**), ATR-FTIR (**S8**), PL (**S9**), achromatic XPS (**S11**)); molecular synthesis (**S12**) with detailed descriptions of experimental procedures and supplementary figures and tables (FTIR, EA, ESI-MS, NMR (^{1}H, ^{13}C, and ^{31}P), UV/Vis).

AUTHOR INFORMATION

Corresponding Author

*johannes.bartl@tum.de, christopher.thomas@tum.de

Present Addresses

[&]Physics Department E59, Technische Universität München, James-Franck-Str.1, 85748 Garching bei München, Germany

[~]Helmholtz-Zentrum Berlin für Materialien and Energie GmbH, BESSY II, Albert-Einstein-Straβe 15, 12489 Berlin, Germany and Haber-Institute der Max Plack Gesellschaft, Dept. Inorganic Chemistry, Faradayweg 4-6, 14195 Berlin, Germany

Author Contributions

All authors have given approval to the final version of the manuscript. [‖]These authors contributed equally.

Funding Sources

This work was supported by the Deutsche Forschungsgemeinschaft (DFG, German Research Foundation) through the TUM International Graduate School of Science and Engineering (IGSSE), by the DFG under Germany's Excellence Strategy (EXC 2089/1-390776260 (e-conversion)), by the Bundesministerium für Bildung und Forschung (BMBF, Germany) *via* TUM.Solar (033RC021B), and by the Bavarian State Ministry of Science, Research, and Arts through "SolarTechnologies go Hybrid (SolTech)". The research leading to this result has been supported by the project CALIPSOplus under Grant Agreement 730872 from the EU Framework Programme for Research and Innovation HORIZON 2020. AH acknowledges funding from the European Union's Horizon 2020 research and innovation programme under the Marie Skłodowska-Curie grant agreement No 841556. MFO and BN acknowledge financial support by the BMBF, Germany *via* project LUCENT (05K19WMA), through SolTech, and by the DFG through SFB1032 "Nanoagents", projects A06/A07. CO acknowledges financial support as a Max Planck Fellow at the Max Planck Institute for Solid State Research, Stuttgart. ACS acknowledges financial support by the DFG (CA1076/5-1).

Notes

The authors declare no competing financial interest.

ACKNOWLEDGMENT

The authors are grateful to A. Hegele for experimental support with NEXAFS measurements and M. Bissolo, T. Grünleitner, J. Eichhorn for support with SPEM measurements. The authors are thankful to D. Chryssikos, O. Bienek, F. Eckmann, and S. Qian for experimental support. JDB and CT are grateful to P. Feulner and S. Vagin for fruitful discussions. Award of beamtimes at the ELETTRA synchrotron (Trieste, Italy) is gratefully acknowledged.

REFERENCES

(1) Jiang, Y.; Tian, B. Inorganic semiconductor biointerfaces. *Nat. Rev. Mater.* **2018** *3*, 473–490.

(2) Diercks, C.S.; Liu, Y.; Cordova, K.E.; Yaghi, O. M. The role of reticular chemistry in the design of CO_2 reduction catalysts. *Nat. Mater.* **2018**, *17*, 301-307.

(3) O'Regan, B.; Grätzel, M. A Low-Cost, High-Efficiency Solar Cell Based on Dye-Sensitized Colloidal TiO_2 Films. *Nature* **1991**, *353*, 737-740.

(4) Xu, C.; Yang, W.; Ren, Z.; Dai, D.; Guo, Q.; Minton, T. K.; Yang, X. Strong Photon Energy Dependence of the Photocatalytic Dissociation Rate of Methanol on TiO_2(110). *J. Am. Chem. Soc.* **2013**, *135*, 19039-19045.

(5) Jeong, K. S.; Pensack, R. D.; Asbury, J. B. Vibrational Spectroscopy of Electronic Processes in Emerging Photovoltaic Materials. *Acc. Chem. Res.* **2013**, *46*, 1538-1547.

(6) Teplyakov, A. V.; Bent, S. F. Semiconductor surface functionalization for advances in electronics, energy conversion, and dynamic systems. *J. Vac. Sci. Technol., A* **2013***, 31*, 050810.

(7) Bent, S. F.; Kachian, J. S.; Rodríguez-Reyes, J. C. F.; Teplyakov, A. V. Tuning the reactivity of semiconductor surfaces by functionalization with amines of different basicity. *Proc. Natl. Acad. Sci.* **2011***, 108*, 956-960.

(8) Vilan, A.; Cahen, D. Chemical Modification of Semiconductor Surfaces for Molecular Electronics. *Chem. Rev.* **2017**, *117*, 4624-4666.

(9) Wieszczycka, K.; Staszak, K.; Woźniak-Budych, M. J.; Litowczenko, J.; Maciejewska, B. M.; Jurga, S. Surface functionalization – The way for advanced applications of smart materials. *Coord. Chem. Rev.* **2021**, *436*, 213846.

(10) Peczonczyk, S. L.; Mukherjee, J.; Carim, A. I.; Maldonado, S. Wet Chemical Functionalization of III–V Semiconductor Surfaces: Alkylation of Gallium Arsenide and Gallium Nitride by a Grignard Reaction Sequence. *Langmuir* **2012**, *28*, 4672-4682.

(11) Lee, S. H.; Kang, J. S.; Kim, D. A Mini Review: Recent Advances in Surface Modification of Porous Silicon. *Materials* **2018**, *11(12)*, 2557.

(12) Meng, X. An overview of molecular layer deposition for organic and organic–inorganic hybrid materials: mechanisms, growth characteristics, and promising applications. *J. Mater. Chem. A* **2017***, 5*, 18326-18378.

(13) Garrido-Diez, D.; Baraia, I. Review of wide bandgap materials and their impact in new power devices. ECMSM 2017, 1-6.

(14) Deckers, J.; Cornagliotti, E.; Debucquoy, M.; Gordon, I.; Mertens, R.; Poortmans, J. Aluminum Oxide-aluminum Stacks for Contact Passivation in Silicon Solar Cells. Energy Procedia **2014**, *55*, 656-664.

(15) Schmidt, J.; Veith, B.; Werner, F.; Zielke, D.; Brendel, R. Silicon surface passivation by ultrathin Al_2O_3 films and Al_2O_3/SiN_x stacks. (IEEE) **2010**, 000885-000890.

(16) Brinkmann, K. O.; Gahlmann, T.; Riedl, T. Atomic Layer Deposition of Functional Layers in Planar Perovskite Solar Cells. *Solar RRL* **2020***, 4*, 1900332.

(17) Martinson, A. B. F.; Elam, J. W.; Hupp, J. T.; Pellin, M. J. ZnO Nanotube Based Dye-Sensitized Solar Cells. *Nano Lett.* **2007**, 7, 2183-2187.

(18) Hoffeditz, W. L.; Son, H.-J.; Pellin, M. J.; Farha, O. K.; Hupp, J. T. Engendering Long-Term Air and Light Stability of a TiO_2-Supported Porphyrinic Dye via Atomic Layer Deposition. ACS Appl. *Mater. Interfaces* **2016**, *8*, 34863-34869.

(19) Veronese, L.; Procopio, E. Q.; De Rossi, F.; Brown, T. M.; Mercandelli, P.; Mussini, P.; D'Alfonso, G.; Panigati, M. New dinuclear hydrido-carbonyl rhenium complexes designed as photosensitizers in dye-sensitized solar cells. *New J. Chem.* **2016**, *40*, 2910-2919.

(20) Sharma, K.; Sharma, V.; Sharma, S. S. Dye-Sensitized Solar Cells: Fundamentals and Current Status. *Nanoscale Res. Lett.* **2018**, *13*, 381.

(21) Cattani-Scholz, A. Functional Organophosphonate Interfaces for Nanotechnology: A Review. *ACS Appl. Mater. Interfaces* **2017**, *9*, 25643-25655.

(22) Hanson, E. L.; Schwartz, J.; Nickel, B.; Koch, N.; Danisman, M. F. Bonding Self-Assembled, Compact Organophosphonate Monolayers to the Native Oxide Surface of Silicon. *J. Am. Chem. Soc.* **2003***, 125*, 16074-16080.

(23) Hanson, E. L.; Guo, J.; Koch, N.; Schwartz, J.; Bernasek, S. L. Advanced Surface Modification of Indium Tin Oxide for Improved Charge Injection in Organic Devices. *J. Am. Chem. Soc.* **2005**, *127*, 10058-10062.

(24) Adden, N.; Gamble, L. J.; Castner, D. G.; Hoffmann, A.; Gross, G.; Menzel, H. Phosphonic Acid Monolayers for Binding of Bioactive Molecules to Titanium Surfaces. *Langmuir* **2006**, *22*, 8197-8204.

(25) Hotchkiss, P. J.; Malicki, M.; Giordano, A. J.; Armstrong, N. R., Marder, S. R. Characterization of phosphonic acid binding to zinc oxide. *J. Mater. Chem.* **2011**, *21*, 3107-3112.

(26) Zhao, R.; Rupper, P.; Gaan, S. Recent Development in Phosphonic Acid-Based Organic Coatings on Aluminum. *Coatings* **2017**, *7*, 133.

(27) Ringk, A.; Li, X.; Gholamrezaie, F.; Smits, E. C. P.; Neuhold, A.; Moser, A.; Van der Marel, C.; Gelinck, G. H.; Resel, R.; de Leeuw, D. M.; Strohriegl, P. N-Type Self-Assembled Monolayer Field-Effect Transistors and Complementary Inverters. *Adv. Funct. Mater.* **2013**, *23*, 2016-2023.

(28) Laibinis, P. E., Hickman, J. J.; Wrighton, M. S.; Whitesides, G. M. Orthogonal self-assembled monolayers: alkanethiols on gold and alkane carboxylic acids on alumina. *Science* **1989**, *245(4920)*, 845-847.

(29) Nebhani, L.; Barner-Kowollik, C. Orthogonal Transformations on Solid Substrates: Efficient Avenues to Surface Modification. *Adv. Mater.* **2009**, *21*, 3442-3468.

(30) Hawecker, J.; Lehn, J.-M.; Ziessel, R. Photochemical and Electrochemical Reduction of Carbon Dioxide to Carbon Monoxide Mediated by (2,2′-Bipyridine)tricarbonylchlororhenium(I) and Related Complexes as Homogeneous Catalysts. *Helv. Chim. Acta* **1986**, *69*, 1990-2012.

(31) Stanley, P. M.; Thomas, C.; Thyrhaug, E.; Urstoeger, A.; Schuster, M.; Hauer, J.; Rieger, B.; Warnan, J.; Fischer, R. A. Entrapped Molecular Photocatalyst and Photosensitizer in Metal–Organic Framework Nanoreactors for Enhanced Solar CO_2 Reduction. *ACS Catalysis* **2021**, *11*, 871-882.

(32) Clark, M. L.; Ge, A.; Videla, P. E.; Rudshteyn, B.; Miller, C. J.; Song, J.; Batista, V. S.; Lian, T.; Kubiak, C. P. CO_2 Reduction Catalysts on Gold Electrode Surfaces Influenced by Large Electric Fields. *J. Am. Chem. Soc.* **2018**, *140*, 17643-17655.

(33) Veronese, L.; Procopio, E. Q.; De Rossi, F.; Brown, T. M.; Mercandelli, P.; Mussini, P.; D'Alfonso, G.; Panigati, M. New dinuclear hydrido-carbonyl rhenium complexes designed as photosensitizers in dye-sensitized solar cells. *New J. Chem.* **2016**, *40*, 2910-2919.

(34) Veronese, L.; Procopio, E.Q.; Moehl, T.; Panigati, M.; Nonomura, K.; Hagfeldt, A. Triarylamine-based hydrido-carboxylate rhenium(i) complexes as photosensitizers for dye-sensitized solar cells. *Phys. Chem. Chem. Phys.* **2019**, *21*, 7534-7543.

(35) Carreño, A.; Solís-Céspedes, E.; Zúñiga, C.; Nevermann, J.; Rivera-Zaldívar, M. M.; Gacitúa, M.; Ramírez-Osorio, A.; Páez-Hernández, D.; Arratia-Pérez, R.; Fuentes, J. A. Cyclic voltammetry, relativistic DFT calculations and biological test of cytotoxicity in walled-cell models of two classical rhenium (I) tricarbonyl complexes with 5-amine-1,10-phenanthroline. *Chem. Phys. Lett.* **2019***, 715*, 231-238.

(36) Coleman, A.; Brennan, C.; Vos, J. G.; Pryce, M. T. Photophysical properties and applications of Re(I) and Re(I)–Ru(II) carbonyl polypyridyl complexes. *Coord. Chem. Rev.,* **2008***, 252*, 2585-2595.

(37) Paoprasert, P.; Laaser, J. E.; Xiong, W.; Franking, R. A.; Hamers, R. J.; Zanni, M. T.; Schmidt, J. R.; Gopalan, P. Bridge-Dependent Interfacial Electron Transfer from Rhenium−Bipyridine Complexes to TiO_2 Nanocrystalline Thin Films. *J. Phys. Chem. C* **2010***, 114*, 9898-9907.

(38) Oudenhoven, T. A.; Joo, Y.; Laaser, J. E.; Gopalan, P.; Zanni, M. T. Dye aggregation identified by vibrational coupling using 2D IR spectroscopy. *J. Chem. Phys.* **2015**, *142*, 212449.

(39) Alam, A. U.; Howlader, M. M. R.; Deen, M. J. The effects of oxygen plasma and humidity on surface roughness, water contact angle and hardness of silicon, silicon dioxide and glass. *J. Micromech. Microeng*. **2014**, 24, 035010.

(40) Tao, Y. T. Structural comparison of self-assembled monolayers of n-alkanoic acids on the surfaces of silver, copper, and aluminum. *J. Am. Chem. Soc.* **1993**, *115*, 4350-4358.

(41) Fukuda, K.; Hamamoto, T.; Yokota, T.; Sekitani, T.; Zschieschang, U.; Klauk, H.; Someya, T. Effects of the alkyl chain length in phosphonic acid self-assembled monolayer gate dielectrics on the performance and stability of low-voltage organic thin-film transistors. *Appl. Phys. Lett.* **2009**, *95*, 203301.

(42) Benson, E. E.; Kubiak, C. P. Structural investigations into the deactivation pathway of the CO_2 reduction electrocatalyst $Re(bpy)(CO)_3Cl$. *Chem. Commun.* **2012***, 48*, 7374-7376.

(43) D'Andre, S. C.; Fadeev, A. Y. Covalent Surface Modification of Calcium Hydroxyapatite Using n-Alkyl- and n-Fluoroalkylphosphonic Acids. *Langmuir* **2003***, 19*, 7904-7910.

(44) Luschtinetz, R.; Oliveira, A.; Duarte, H.; Seifert, G. Self-assembled Monolayers of Alkylphosphonic Acids on Aluminum Oxide Surfaces – A Theoretical Study. *Z. anorg. allg. Chem.* **2010***, 636*, 1506-1512.

(45) Puurunen, R. L. Surface chemistry of atomic layer deposition: A case study for the trimethylaluminum/water process. *Int. J. Appl. Phys.* **2005***, 97*, 121301.

(46) Henning, A.; Bartl, J. D.; Zeidler, A.; Qian, S.; Bienek, O.; Jiang, C.-M.; Paulus, C.; Rieger, B.; Stutzmann, M., Sharp, I. D. Aluminum Oxide at the Monolayer Limit via Oxidant-Free Plasma-Assisted Atomic Layer Deposition on GaN. *Adv. Funct. Mater.* **2021**, 2101441.

(47) Wagner, C.D.; Naumkin, A.V.; Kraut-Vass, A.; Allison, J.W.; Powell, C.J.; Rumble, J.R.Jr. NIST Standard Reference Database 20, Version 3.4 (web version), 2003; available from https://srdata.nist.gov/xps/Default.aspx (accessed: 16.6.2021).

(48) Barrie, A.; Drummond, I.; Herd, Q. Correlation of calculated and measured 2p spin-orbit splitting by electron spectroscopy using monochromatic x-radiation. *J. Electron Spectros. Relat. Phenomena* **1974**, *5*, 217-225.

(49) Wagstaffe, M.; Thomas, A. G.; Jackman, M. J.; Torres-Molina, M.; Syres, K. L.; Handrup, K. An Experimental Investigation of the Adsorption of a Phosphonic Acid on the Anatase TiO2(101) Surface. *J. Phys. Chem. C* **2016***, 120*, 1693-1700.

(50) Schuschke, C.; Schwarz, M.; Hohner, C.; Silva, T. N.; Fromm, L.; Döpper, T.; Görling, A.; Libuda, J. Phosphonic Acids on an Atomically Defined Oxide Surface: The Binding Motif Changes with Surface Coverage. *J. Phys. Chem. Lett.* **2018***, 9*, 1937-1943.

(51) Gengenbach, T. R.; Major, G. H.; Linford, M. R.; Easton, C. D. Practical guides for x-ray photoelectron spectroscopy (XPS): Interpreting the carbon 1s spectrum. *J. Vac. Sci. Technol. A* **2021***, 39*, 013204.

(52) Greiner, M.; Rocha, T.; Johnson, B.; Klyushin, A.; Knop-Gericke, A.; Schlögl, R. The Oxidation of Rhenium and Identification of Rhenium Oxides During Catalytic Partial Oxidation of Ethylene: An In-Situ XPS Study. *Z. Phys. Chem.* **2014***, 228*, 521-541.

(53) Popov, D. A.; Luna, J. M.; Orchanian, N. M.; Haiges, R.; Downes, C. A.; Marinescu, S. C. A 2,2′-bipyridine-containing covalent organic framework bearing rhenium(i) tricarbonyl moieties for CO_2 reduction. *Dalton Trans.* **2018***, 47*, 17450-17460.

(54) Cabarcos, O. M.; Shaporenko, A.; Weidner, T.; Uppili, S.; Dake, L. S.; Zharnikov, M.; Allara, D. L. Physical and Electronic Structure Effects of Embedded Dipoles in Self-Assembled Monolayers: Characterization of Mid-Chain Ester Functionalized Alkanethiols on Au111. *J. Phys. Chem. C* **2008***, 112*, 10842-10854.

(55) Joo, Y.; Spalenka, J. W.; McElhinny, K. M.; Schmitt, S. K.; Evans, P. G.; Gopalan, P. Structured Layer of Rhenium Dye on SiO2 and TiO2 Surfaces by Langmuir–Blodgett Technique. *Langmuir* **2014***, 30*, 6104-6113.

(56) Beamson, G.; Briggs, D. High Resolution XPS of Organic Polymers the Scienta ESCA300 Database. Wiley, Chichester, 1992, p. 295.

(57) Chadefaux, C.; Le Hô, A.-S.; Bellot-Gurlet, L, Reiche, I. Curve-fitting micro-ATR-FTIR studies of the amide I and II bands of type I collagen in archaeological bone materials. *e-PS* **2009**, *6*, 129-137.

(58) Laaser, J. E.; Christianson, J. R.; Oudenhoven, T. A.; Joo, Y.; Gopalan, P.; Schmidt, J. R.; Zanni, M. T. Dye Self-Association Identified by Intermolecular Couplings between Vibrational Modes As Revealed by Infrared Spectroscopy, and Implications for Electron Injection. *J. Phys. Chem. C* **2014***, 118*, 5854-5861.

(59) Cantero-López, P.; Hidalgo-Rosa, Y.; Sandoval-Olivares, Z.; Santoyo-Flores, J.; Mella, P.; Arrué, L.; Zúñiga, C.; Arratia-Pérez, R.; Páez-Hernández, D.The role of zero-field splitting and π-stacking interaction of different nitrogen-donor ligands on the optical properties of luminescent rhenium tricarbonyl complexes. *New J. Chem.* **2021**, *45*, 11192-11201.

(60) Sakamoto, R.; Katagiri, S.; Maeda, H.; Nishimori, Y.; Miyashita, S.; Nishihara, H. Electron Transport Dynamics in Redox-Molecule-Terminated Branched Oligomer Wires on Au(111). *J. Am. Chem. Soc.* **2015**, *137*, 734-741.

(61) Singh, A. P.; Samuel, P. P.; Roesky, H. W.; Schwarzer, M. C.; Frenking, G.; Sidhu, N. S.; Dittrich, B. A Singlet Biradicaloid Zinc Compound and Its Nonradical Counterpart. *J. Am. Chem. Soc.* **2013**, *135*, 7324-7329.

(62) Cancelliere, A. M.; Puntoriero, F.; Serroni, S.; Campagna, S.; Tamaki, Y.; Saito, D., Ishitani, O. Efficient trinuclear Ru(ii)–Re(i) supramolecular photocatalysts for CO_2 reduction based on a new tris-chelating bridging ligand built around a central aromatic ring. *Chem. Sci.* **2020**, *11*, 1556-1563.

(63) Wang, L.; Schubert, U. S.; Hoeppener, S. Surface chemical reactions on self-assembled silane based monolayers. *Chem. Soc. Rev.* **2021**, *50*, 6507-6540.

(64) Herzer, N.; Hoeppener, S.; Schubert, U. S. Fabrication of patterned silane based self-assembled monolayers by photolithography and surface reactions on silicon-oxide substrates. *Chem. Commun.* **2010**, *46*, 5634-5652.

(65) Cottineau, T.; Morin, M.; Bélanger, D. Surface band structure of aryl-diazonium modified p-Si electrodes determined by X-ray photoelectron spectroscopy and electrochemical measurements. *RSC Adv.* **2013***, 3*, 23649-23657.

(66) Ahoulou, S.; Perret, E.; Nedelec, J.-M. Functionalization and Characterization of Silicon Nanowires for Sensing Applications: A Review. *Nanomaterials* **2021**, *11*, 999.

(67) Khan, M.; Rao, M. V. Gallium Nitride (GaN) Nanostructures and Their Gas Sensing Properties: A Review. *Sensors* **2020**, *20(14)*, 3889.

(68) Pfennig, B. W.; Chen, P.; Meyer, T. J. Photophysics and Photochemistry of Chromophore−Quencher Assemblies on Glass and Powdered Silica. Inorg. Chem. **1996**, *35*, 2898-2901.

(69) Neises, B.; Steglich, W. Simple Method for the Esterification of Carboxylic Acids. *Angew. Chem.* **1978**, *17*, 522-524.

(70) Blaschke, B. M.; Böhm, P.; Drieschner, S.; Nickel, B.; Garrido, J. A. Lipid Monolayer Formation and Lipid Exchange Monitored by a Graphene Field-Effect Transistor. *Langmuir,* **2018***, 34*, 4224-4233.

(71) Nelson, A. R. J.; Prescott, S. W. refnx: neutron and X-ray reflectometry analysis in Python. *J. Appl. Crystallogr.* **2019**, *52*, 193-200.

(72) Zangrando, M.; Finazzi, M.; Paolucci, G.; Comelli, G.; Diviacco, B.; Walker, R. P.; Cocco, D.; Parmigiani, F. BACH, the beamline for advanced dichroic and scattering experiments at ELETTRA. *Rev. Sci. Instrum.* **2001**, *72*, 1313-1319.

(73) Zeller, P.; Amati, M.; Sezen, H.; Scardamaglia, M.; Struzzi, C.; Bittencourt, C.; Lantz, G.; Hajlaoui, M.; Papalazarou, E.; Marino, M.; Fanetti, M.; Ambrosini, S.; Rubini, S.; Gregoratti, L. Scanning Photoelectron Spectro-Microscopy: A Modern Tool for the Study of Materials at the Nanoscale. *Phys. Status Solidi A* **2018**, *215*, 1800308/1-8.

(74) Ernzerhof, M.; Scuseria, G. E. Assessment of the Perdew-Burke-Ernzerhof exchange-correlation functional. *J. Chem. Phys.* **1999***, 110*, 5029-5036.

(75) Adamo, C.; Barone, V. Toward reliable density functional methods without adjustable parameters: The PBE0 model. *J. Chem. Phys.* **1999***, 110*, 6158-6170.

(76) Grimme, S.; Antony, J.; Ehrlich, S.; Krieg, H. A consistent and accurate ab initio parametrization of density functional dispersion correction (DFT-D) for the 94 elements H-Pu. *J. Chem. Phys.* **2010***, 132*, 154104.

(77) Schäfer, A.; Huber, C.; Ahlrichs, R. Fully optimized contracted Gaussian basis sets of triple zeta valence quality for atoms Li to Kr. *J. Chem. Phys.* **1994***, 100*, 5829-5835.

(78) TURBOMOLE V7.3 2018, a development of University of Karlsruhe and Forschungszentrum Karlsruhe GmbH, 1989–2007, TURBOMOLE GmbH, since 2007; available from http://www.turbomole.com.

(79) Ahlrichs, R.; Bär, M.; Häser, M.; Horn, H.; Kölmel, C. Electronic structure calculations on workstation computers: The program system turbomole. *Chem. Phys. Lett.* **1989**, *162*, 165-169.

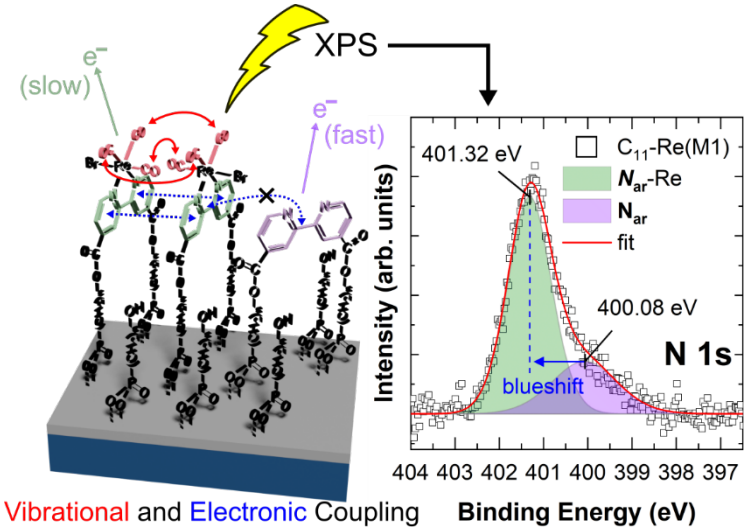
XPS
e⁻
(slow)
e⁻
(fast)
401.32 eV
C11-Re(M1)
Nar-Re
Nar
fit
400.08 eV
N 1s
blueshift
Intensity (arb. units)
404 403 402 401 400 399 398 397
Vibrational and Electronic Coupling
Binding Energy (eV)